

Dwarf AGNs from Variability for the Origins of Seeds (DAVOS): Optical Variability of Broad-line Dwarf AGNs from the Zwicky Transient Facility

Z. Franklin Wang,^{1,2,3*} Colin J. Burke,^{1†} Xin Liu,^{1,4} Yue Shen^{1,4}

¹Department of Astronomy, University of Illinois at Urbana-Champaign, 1002 West Green Street, Urbana, IL 61801, USA

²Department of Physics and Astronomy, Texas A&M University, College Station, TX 77843-4242, USA

³George P. and Cynthia Woods Mitchell Institute for Fundamental Physics and Astronomy, Texas A&M University, College Station, TX 77843-4242, USA

⁴National Center for Supercomputing Applications, 1205 West Clark Street, Urbana, IL 61801, USA

arXiv:2212.02321v1 [astro-ph.GA] 5 Dec 2022

Accepted XXX. Received YYY; in original form ZZZ

ABSTRACT

We study the optical variability of a sample of candidate low-mass (dwarf and Seyfert) active galactic nuclei (AGNs) using Zwicky Transient Facility *g*-band light curves. Our sample is compiled from broad-line AGNs in dwarf galaxies reported in the literature with single-epoch virial black hole (BH) masses in the range $M_{\text{BH}} \sim 10^4 - 10^8 M_{\odot}$. We measure the characteristic “damping” timescale of the optical variability τ_{DRW} , beyond which the power spectral density flattens, of a final sample of 79 candidate low-mass AGNs with high-quality light curves. Our results provide further confirmation of the $M_{\text{BH}} - \tau_{\text{DRW}}$ relation from Burke et al. (2022) within 1σ agreement, adding 78 new low-mass AGNs to the relation. The agreement suggests that the virial BH mass estimates for these AGNs are generally reasonable. We expect that the optical light curve of an accreting intermediate-mass black hole (IMBH) to vary with a rest-frame damping timescale of \sim tens of hours, which could enable detection and direct mass estimation of accreting IMBHs in wide-field time-domain imaging surveys with sufficient cadence like with the Vera C. Rubin Observatory.

Key words: black hole physics, accretion, accretion discs, galaxies: dwarf, galaxies: active

1 INTRODUCTION

Intermediate-mass black holes (IMBHs; $M_{\text{BH}} = 10^2 - 10^5 M_{\odot}$) are thought to be the missing link between stellar-mass and supermassive black holes (SMBHs). The demographics of active galactic nuclei (AGN) in dwarf galaxies hosting IMBHs traces the formation mechanisms of SMBH seeds which are believed to have formed in nascent galaxies at high redshift (e.g., Volonteri 2010; Reines & Comastri 2016; Greene et al. 2020; Inayoshi et al. 2020). Perhaps the best observational evidence for IMBHs is the gravitational wave event GW190521 from the merger of two black holes (with a remnant mass of $142^{+28}_{-16} M_{\odot}$; LIGO Scientific Collaboration & Virgo Collaboration 2020). Accreting IMBHs remain difficult to identify, with only a few exceptional candidates such as the X-ray tidal disruption event 3XMM J215022.4-055108 (Lin et al. 2018); and the $M_{\text{BH}} \sim 10^4 M_{\odot}$ hyper-luminous X-ray source ESO 243-49 HLX-1 (Farrell et al. 2009).

Recent works demonstrated success in identifying dwarf AGNs with BH masses on the boundary between IMBHs and SMBHs with $M_{\text{BH}} \sim 10^4 - 10^6 M_{\odot}$ using optical spectroscopic signatures (e.g., Greene & Ho 2005; Reines et al. 2013; Baldassare et al. 2015, 2016; Cann et al. 2020) or variability (e.g., Baldassare et al. 2018, 2020; Martínez-Palomera et al. 2020; Guo et al. 2020; Ward et al. 2022; Burke et al. 2022). We have compiled a parent sample of dwarf

AGN candidates in the literature with optical signatures of accretion activity (variability, narrow emission line diagnostics, and/or broad emission lines). Then, we restricted our sample to broad-line AGNs and those with virial BH mass estimates. These virial BH masses are in the range $M_{\text{BH}} \sim 10^4 - 10^6 M_{\odot}$ (Greene & Ho 2007; Chilingarian et al. 2018; Liu et al. 2018). We add the sample of low-mass (dwarf and Seyfert) AGNs with $M_{\text{BH}} \sim 10^5 - 10^8 M_{\odot}$ from Reines & Volonteri 2015 used to calibrate their local BH - host galaxy stellar mass relation, because we will attempt to benchmark our variability timescale -derived BH masses against the Reines & Volonteri 2015 relation. These low-mass AGNs offer the best cases currently to test our understanding of accretion physics close to the IMBH regime.

Optical variability in AGN light curves can be used to probe accretion disk structure and the dominant physical processes at the radius of optical emission. The power spectral density (PSD) of optical AGN light curves are well-described by a damped random walk (DRW) model from hours to years timescales, where the PSD transitions from white noise to red noise (f^{-2}) at a characteristic frequency ($f_{\text{DRW}} = (2\pi\tau_{\text{DRW}})^{-1}$) (e.g., Kelly et al. 2009; MacLeod et al. 2010). The corresponding rest-frame “damping” timescale τ_{DRW} correlates strongly with M_{BH} and is likely associated with the thermal timescale in the accretion disk at the UV-emitting radius (Burke et al. 2021). Ward et al. (2022) found evidence that their sample of variability-selected dwarf AGNs have more rapid variability compared to a control sample of massive AGNs using ZTF light curves.

The $M_{\text{BH}} - \tau_{\text{DRW}}$ relation of Burke et al. (2021) predicts a τ_{DRW}

* E-mail: zfwang2@tamu.edu (ZFW)

† E-mail: colinjb2@illinois.edu (CJB)

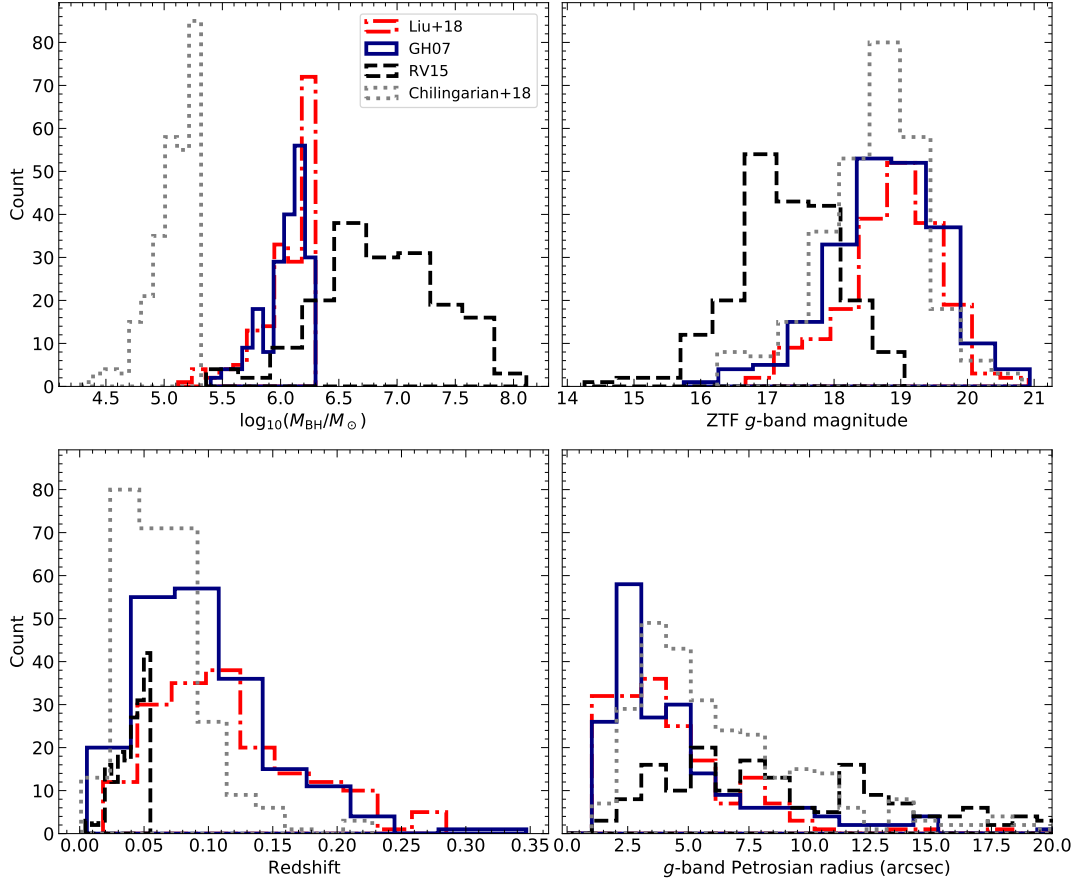


Figure 1. Distributions of the virial BH mass estimates (*top left*), ZTF g -band PSF magnitude (*top right*), spectroscopic redshift (*bottom left*), and g -band Petrosian radius (*bottom right*) for our parent sample of low-mass AGNs selected from Greene & Ho (2007) ("GH07"), Reines & Volonteri (2015) ("RV15"), Chilingarian et al. (2018) ("Chilingarian+18"), and Liu et al. (2018) ("Liu+18").

of tens of days for a $10^6 M_{\odot}$ BH as opposed to several hundred days for a $10^9 M_{\odot}$ SMBH. Therefore, the variability timescales for dwarf AGNs are well-sampled by Zwicky Transient Facility (ZTF; Masci et al. 2019; Bellm et al. 2019) light curves with a typical baseline and cadence of ~ 1000 days and ~ 3 days respectively. We will test the $M_{\text{BH}} - \tau_{\text{DRW}}$ relation in the dwarf AGN regime, motivated by the possibility of extrapolating the relation to even lower masses to enable not only IMBH discovery, but also host-independent BH mass estimation, which may not be feasible with traditional spectroscopy-based methods due to the lack of broad emission lines (Chakravorty et al. 2014).

In this work, we report our time series analysis of ZTF light curves of 79 low-mass AGNs with virial BH mass estimates of $10^{5.69} \leq M_{\text{BH}}(M_{\odot}) \leq 10^{7.80}$. We focus on spectroscopically-confirmed broad-line dwarf AGNs. This includes 78 new objects which we place on the $M_{\text{BH}} - \tau_{\text{DRW}}$ relation compared to the previous Burke et al. (2021) sample with ~ 4 years long light curves, sufficient to constrain the damping timescale for dwarf AGNs. These objects were not included in the Burke et al. (2021) sample, which only considered objects from Reines et al. (2013) and used a previous ZTF data release with shorter light curve lengths of ~ 2 years. We describe the AGN parent sample and data in §2, present our results in §3, discuss the possible implications in §4, and conclude in §5. All uncertainties and plotted error bars are 1σ unless otherwise specified.

2 OBSERVATIONS AND DATA ANALYSIS

2.1 Dwarf AGN Parent Sample

We searched the literature for dwarf AGN candidates with broad-line measurements that enabled single-epoch virial BH mass estimates (Shen 2013). Our parent sample of low-mass AGNs come from the following sources: Greene & Ho (2007) ("GH07"), Reines & Volonteri (2015) ("RV15"), Chilingarian et al. (2018) ("Chilingarian+18"), and Liu et al. (2018) ("Liu+18"). These AGNs were identified using one of two methods. First, dwarf galaxies were identified with narrow emission line ratios consistent with an AGN based on the classical BPT diagram (Baldwin et al. 1981; Veilleux & Osterbrock 1987; Kewley et al. 2006) with broad emission lines detected afterwards. Second, AGNs were selected via detection of the broad emission line itself from Sloan Digital Sky Survey (SDSS) spectra (York et al. 2000; Abazajian et al. 2009) even if the line ratios are consistent with star-formation. In the later case, the broad emission lines can be due to a supernova or stellar transient, requiring follow-up observations years later (Baldassare et al. 2016). However, long-duration variability can also be used to test the AGN scenario. In this work, we only included sources with published BH masses from broad emission line detections with persistent, AGN-like variability. We show the virial BH mass estimate, g -band PSF magnitude, spectroscopic redshift, and host-galaxy g -band Petrosian radii (Petrosian 1976; Graham et al. 2005) distributions for the parent sample sources in Figure 1. We checked for duplicate sources between the samples,

and used the M_{BH} value from the more recent publication in those cases.

2.2 Light Curve Data and Cleaning

ZTF is a time-domain optical (primarily g and r with some i -band) imaging survey using the Samuel Oschin 48-inch Schmidt telescope at Palomar Observatory. ZTF light curves began in 2018 with a nominal cadence of 2 or 3 days (with seasonal gaps), covering declinations above -30 degrees with a single-epoch imaging depth of 20.5 mag (5σ , r band). The ZTF data release light curves are PSF-based, and will introduce additional measurement error for resolved sources given the median g -band PSF full width at half maximum (FWHM) of $2''.1$ (Bellm et al. 2019). For this reason, we use difference imaging-based photometry as described below.

We downloaded difference images from the ZTF data release 13 (March 2018 – July 2022) in the g band from the NASA/IPAC Infrared Science Archive¹ which had coverage of any one of our sample targets. After collecting the images, we extracted photometry using a $2''.5$ diameter aperture, which is well-matched to the ZTF seeing, using the PHOTUTILS code (Bradley et al. 2022). After constructing the light curves, we performed outlier rejection at the 3σ level using a moving window size of 1 year. Given AGNs tend to be more variable in at bluer wavelengths, we restrict our analysis to the g band. This effect may be even stronger for dwarf AGNs, as the disk temperature of an IMBH shifts the SED into the UV (e.g., Cann et al. 2018).

2.3 Light Curve Modeling

It has become increasingly popular to model AGN light curves in the time domain (as opposed to the frequency domain) with a Continuous Auto-Regressive Moving Average (CARMA) model (e.g., Kelly et al. 2009, 2014; Simm et al. 2016; Suberlak et al. 2021). The CARMA models are a set of flexible Gaussian process models (Aigrain & Foreman-Mackey 2022) to describe stochastic time series, with two parameters, p and q , describing the orders of the auto-regression (AR) part and the moving average (MA) part. The DRW model is the lowest order CARMA model with $p = 1$ and $q = 0$, or a CAR(1) process. In this work we use the DRW model to constrain the characteristic damping timescale of an AGN light curve. Deviations from the simple DRW model for SMBHs have been reported on short timescales with space- or ground-based photometry (e.g., Mushotzky et al. 2011; Kasliwal et al. 2015; Stone et al. 2022). To check that the DRW model is sufficient for our data, we visually confirmed that the ACF of the χ^2 (model–data) residuals are consistent with Gaussian white noise using Bartlett’s formula. Given that the best-fitting DRW models have sufficiently small residuals, higher-order CARMA models are not justified given the data quality. Burke et al. (2021) provided a more detailed discussion on the advantages and caveats of the DRW model compared with the more complicated higher-order CARMA models.

The major advantage of the Gaussian process models is that they can provide an accurate description of irregularly-sampled stochastic light curves and the underlying PSD while taking into account measurement uncertainties. Because the modeling is performed in the time domain rather than in the frequency domain, the inferred PSD is more robust against windowing effects (such as aliasing and red noise leakage) than traditional power spectral analysis. Fitting a broken power law to the PSD of light curves can produce consistent

results with time domain DRW fitting, albeit with larger intrinsic scatter and greater demands on the light curve sampling and quality (Burke et al. 2021). We compute the PSD using the Lomb–Scargle periodogram (Lomb 1976; Scargle 1982) as a consistency check. A typical example of our time series analysis and DRW fitting is shown in Figure 2. The light curves and their best-fit DRW models of our final sample are shown in Appendix A.

The covariance function for a DRW plus extra white noise model is,

$$k(t_{nm}) = 2\sigma_{\text{DRW}}^2 \exp(-t_{nm}/\tau_{\text{DRW}}) + \sigma_n^2 \delta_{nm} \quad (1)$$

where $t_{nm} = |t_n - t_m|$ is the time lag between measurements m and n , σ_{DRW} is the amplitude term, τ_{DRW} is the damping timescale, σ_n is the white noise amplitude, and δ_{nm} is the Kronecker δ function. We include the white noise term to account for excess measurement noise in the ZTF light curves due to e.g., seeing variations or underestimated uncertainties from our photometric extraction procedure, which does not include systematic sources of uncertainty in addition to the statistical uncertainties. This model has an exact correspondence to the structure function (SF) definition,

$$\begin{aligned} \text{SF}^2 &= \text{SF}_\infty^2 (1 - \text{ACF}(t_{nm})) \\ &= 2\sigma_{\text{DRW}}^2 (1 - \exp(-t_{nm}/\tau_{\text{DRW}})) \end{aligned} \quad (2)$$

where the asymptotic variability amplitude $\text{SF}_\infty = \sqrt{2}\sigma_{\text{DRW}}$ and the autocorrelation function $\text{ACF}(t_{nm}) = \exp(-t_{nm}/\tau_{\text{DRW}})$. Therefore, we have three free parameters to fit in the model: σ_{DRW} , τ_{DRW} , and σ_n . We use the CELERITE package (Foreman-Mackey et al. 2017) to perform the model fitting. We use Markov chain Monte Carlo (MCMC) implemented in the EMCEE package (Foreman-Mackey et al. 2013) to sample the joint posterior probability density, with uniform priors for all parameters. We take the 16th and 84th percentiles of the marginalized posterior distributions for each parameter to estimate the 1σ uncertainties.

2.4 Recoverability of Input Damping Timescale

Following Burke et al. (2021), we impose the following minimal quality constraints on our light curves for our final sample:

- (i) **Length:** $\tau_{\text{DRW}} < 0.1 \times \text{baseline}$.
- (ii) **Sampling:** $\tau_{\text{DRW}} > 6$ days.
- (iii) **Signal-to-noise ratio (SNR):** $\text{SNR} > 1$, where $\text{SNR} = \sigma_{\text{DRW}} / \sqrt{\sigma_n^2 + \overline{dy}^2}$ where \overline{dy} is the mean uncertainty of the light curve measurements.
- (iv) **AGN-like variability:** $\sigma_{\text{LB}} > 3$, where σ_{LB} is the Ljung–Box test (Ljung & Box 1978) significance under the null hypothesis that the light curve is white noise.

Constraint (i) is required to avoid a bias in the value of τ_{DRW} if the light curve is of insufficient length. If the light curve is too short, the most likely value of the recovered τ_{DRW} is $20 - 30\%$ the light curve length with a large scatter (Kozłowski 2017). Constraint (ii) is required so that the measured damping timescale does not artificially converge near the cadence. Given the uncertainty of a factor of 0.3 dex, we require τ_{DRW} to be a factor of ~ 2 greater than the typical ZTF cadence of 3 days (i.e., $\tau_{\text{DRW}} \lesssim 6$ days could be consistent with fitting noise). Constraint (iii) ensures the fitted model amplitude is reasonable compared to the light curve measurement errors and the DRW SNR is sufficient for a reliable fit. Constraints (iii) and (iv) are both required, because CELERITE will attempt to fit a DRW to a light curve even if it is dominated by measurement noise, resulting in

¹ <https://irsa.ipac.caltech.edu/Missions/ztf.html>

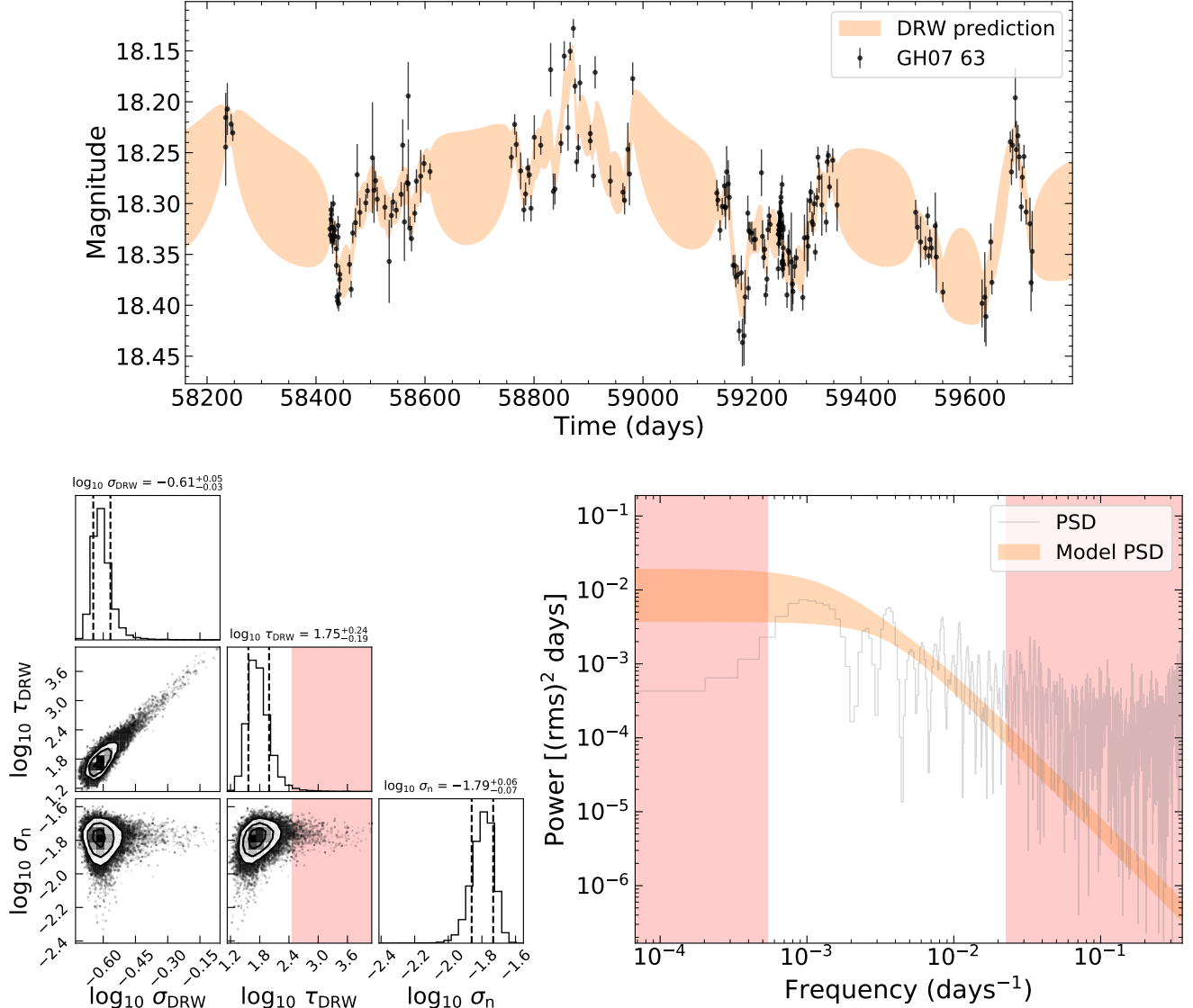


Figure 2. Example DRW modeling of SDSS J090320.97+045738.0 with $M_{\text{BH}} = 10^{6.1} \pm 0.3 M_{\odot}$ and $z = 0.0567$ (Greene & Ho 2007). We show the g -band difference imaging light curve and the best-fit DRW model with 1σ uncertainty (orange shaded area) (top panel). We show the posterior probability distributions for the fitted DRW parameters and their covariance (Equation 1). In the covariance panels, the contours trace the 1, 2, 3 σ levels overplotted on the sample density map (black being higher density) with individual samples in the lowest-density regions shown as black points (bottom left panel). Finally, we show the normalized Lomb-Scargle PSD in gray and the 1σ range of the DRW PSD from the posterior prediction as the orange shaded area (bottom right panel). Note the Lomb-Scargle PSD includes a white noise floor at high frequency that is not included in the DRW model. The red shaded regions correspond to periods greater than 20% the light curve length and less than the mean cadence, where the PSD is not well sampled.

$\text{SNR} > 1$. Both these constraints assure the DRW is properly fitted to a light curve with AGN-like (correlated) variability.

To justify each of the constraints above, we perform DRW simulations to test the recoverability of input τ_{DRW} . For each of the light curves in our g -band parent sample, we create a simulated DRW light with the same sampling/cadence, length, and noise as the real data. For the first test, we use the same amplitude σ_{DRW} and damping timescale τ_{DRW} as the real light curve. Then, we performed a set of simulations in the same fashion with input τ_{DRW} 10 times and 0.1 times the values from the real light curves. Figure 3 shows the results of these simulations. When all quality and duration constraints are applied, the recovered τ_{DRW} are shown to be reliable (blue circles in the central box in the left panel of Figure 3).

In our final sample of 79 low-mass AGN candidates that pass

both our initial criteria (compactness and variability) as well as the DRW model fitting quality checks above (criteria i-iii), we found one object in common with the final Burke et al. (2021) sample. The low-mass end of the Burke et al. (2021) relation is dominated by a few dwarf AGNs from Reines et al. (2013) with shorter light curve durations from a previous ZTF data release and a light curve of NGC 4395 from the Transiting Exoplanet Survey Satellite (Burke et al. 2020). Of the five ZTF sources in the final sample from Burke et al. (2021), we excluded four from this work for the following reasons: Mrk 1044 ($\text{SNR} < 1.0$), NGC 4395 (insufficient cadence/sampling), RGG 127 ($\text{SNR} < 1.0$), and RGG 123 ($\text{SNR} < 1.0$). This does not indicate the Burke et al. (2021) measurements for these sources were incorrect, because in this work we enforced stricter quality controls starting from a larger sample of ZTF light curves. Compared to the

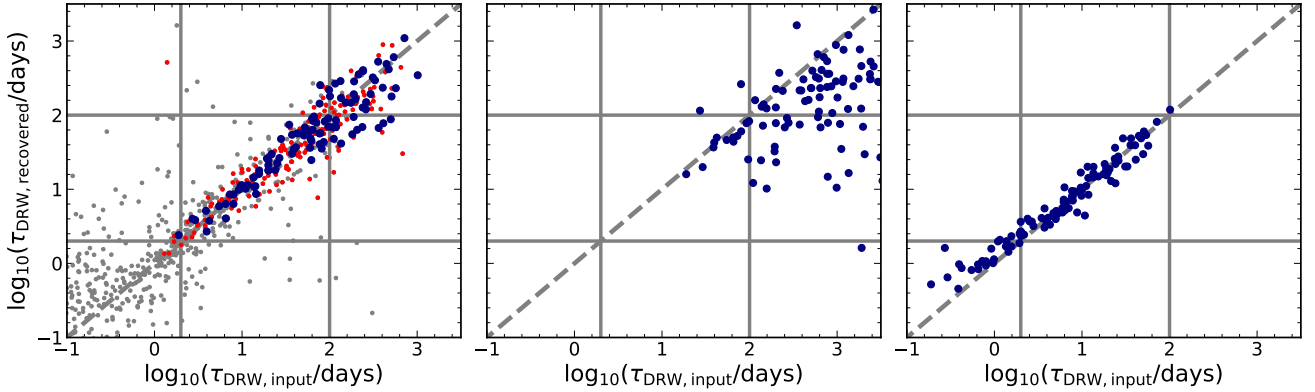


Figure 3. Input versus recovered damping timescale for simulated realistic DRW light curves. *Left panel:* Recoverability using the input τ_{DRW} from our parent sample with no quality constraints (grey points), with constraints (ii) ($\tau_{\text{DRW}} >$ cadence) and (iv) ($\sigma_{\text{LB}} > 3$) (red points), and with constraints (i) (SNR > 1), (ii), and (iii) (blue circles). *Center panel:* Recoverability using input τ_{DRW} of 10 times the result from our parent sample after applying constraints (i), (ii), and (iii) on the original light curves. The recovered τ_{DRW} are biased and saturate at values near 20 – 30% the light curve length when the input τ_{DRW} is greater than about 10% the light curve length. *Right panel:* Recoverability using input τ_{DRW} of 0.1 times the result from our parent sample after applying constraints (i), (ii), and (iii) on the original light curves. Light curves with input τ_{DRW} smaller than the mean cadence typically have unreliable recovered τ_{DRW} . No duration constraints were applied in our simulations to demonstrate the bias for light curves of insufficient duration (Kozłowski 2017). The pair of (vertical or horizontal) gray lines corresponds to the cadence and $0.1 \times$ the light curve length of a typical ZTF light curve in our sample. The dashed gray line shows the $y = x$ line.

previous work, more of our ZTF light curves would pass the length requirement given the longer ZTF light curves from the more recent data release. However, we found that many of those light curves which were too short for inclusion in the final Burke et al. (2021) sample are noisy from e.g., variations in weather across the light curve. Given the much worse average quality of parent AGN sample of ZTF data release light curves, we required stricter quality cuts in this work at a cost of sample completeness. Indeed, visual inspection of the model fitting results for these four sources indicates that the fits may be reasonable and their damping timescale are within 1σ agreement. A summary table of our DRW fitting results for the final sample is given in Table 1.

3 RESULTS

We perform linear regression between τ_{DRW} (rest-frame) and M_{BH} incorporating measurement uncertainties of both quantities. We do not correct for differences between observed wavelength at different redshifts, because the observed scaling of $\tau_{\text{DRW}} \propto \lambda^{0.17}$ (MacLeod et al. 2010; Suberlak et al. 2021; Stone et al. 2022) is generally smaller than the measurement uncertainties given the moderate redshift range of our AGNs. These measurement uncertainties are slightly asymmetric in general, therefore we symmetrize them by taking the mean. We use a hierarchical Bayesian model for fitting a line to data with measurement uncertainties (Kelly 2007). The best-fit relation and 1σ uncertainties for our parent sample of 79 low-mass AGNs follow the simple linear relation,

$$\tau_{\text{DRW}} = \alpha \text{ days} \left(\frac{M_{\text{BH}}}{10^6 M_{\odot}} \right)^{\beta} \quad (3)$$

where $\alpha = 22.19^{+2.66}_{-1.68}$, $\beta = 0.31^{+0.03}_{-0.03}$ with a 1σ intrinsic scatter of $0.20^{+0.03}_{-0.03}$ dex in τ_{DRW} . The data and best-fit relation are shown in Figure 4. Our best-fitting linear model is consistent with the Burke et al. (2021) results within 1σ . However, the dynamic range in BH mass for the sample of dwarf AGNs is small, which results in a much shallower slope with larger uncertainties than the best-fitting relation

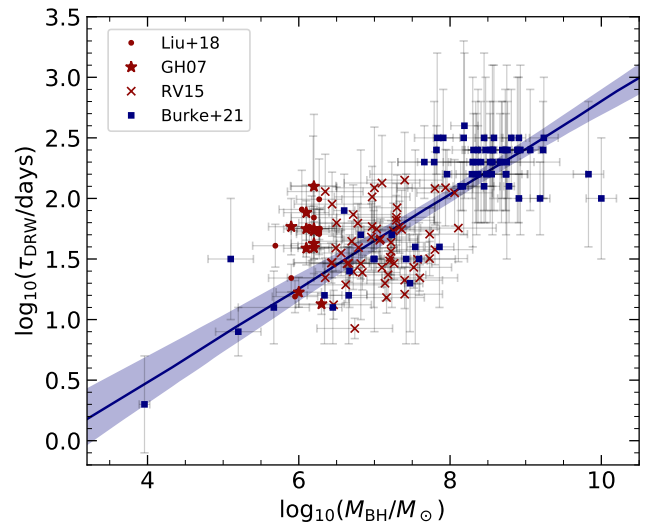


Figure 4. Rest-frame damping timescale versus black hole mass for our final sample (red symbols) with 1σ uncertainty measured using g -band ZTF light curves. We also show the data (blue square symbols) and best-fit relation (blue line) with 1σ uncertainty (light blue band) from Burke et al. (2021). Our best-fit relation is consistent with the relation of Burke et al. (2021) within 1σ .

in Burke et al. (2021). Given the small dynamic range in mass of dwarf AGNs, it is not surprising that a correlation is not statistically significant using our sample alone.

3.1 Extension to Stellar Mass Accretion Disks

Next, we re-fit the combined final sample of g -band ZTF dwarf AGNs with the final sample from Burke et al. (2021). The results are shown in Figure 5. We removed the one g -band duplicate source from the Burke et al. (2021) sample which was included in our sample with

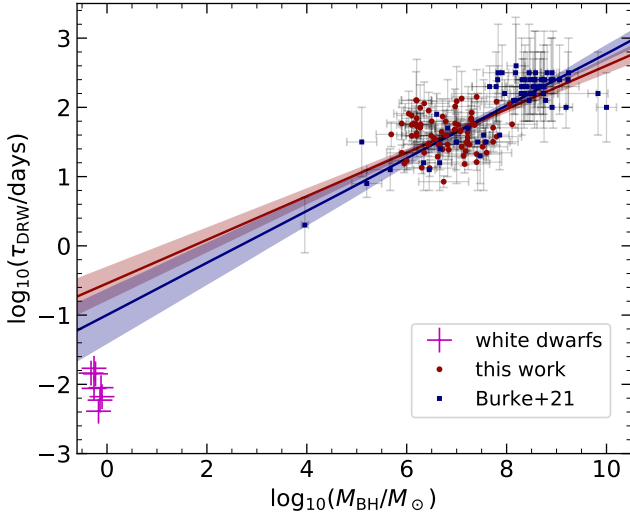


Figure 5. Rest-frame damping timescale versus black hole mass for our final g -band ZTF sample combined with the final sample from Burke et al. (2021) (black symbols). We show the best-fit relation (black line) with 1σ uncertainty (gray band) measured using the combined sample data with duplicate sources removed (see text). We also show the data and best-fit relation (blue line) with 1σ uncertainty (light blue band) from Burke et al. (2021). For comparison, we show the values for accreting white dwarfs (Scaringi et al. 2015), scaled to the typical AGN Eddington luminosity ratio of 0.15, in magenta. The typical uncertainties on M_{WD} and the white dwarf damping timescale are 0.2 dex and 0.01 days respectively (Scaringi et al. 2015).

longer ZTF light curves and updated BH masses from the relation of Reines & Volonteri (2015). For comparison to stellar mass accretion disks, we also show accreting white dwarfs of the nova-like class from Scaringi et al. (2015). However, we do not include the white dwarfs in the fitting. Although our combined sample results appear consistent with previous work, we caution that the ZTF light curves are generally of poorer quality and the virial BH masses of dwarf AGNs may have greater uncertainties, resulting in a larger scatter for these dwarf AGNs. Nevertheless, this provides an important confirmation to the Burke et al. (2021) results after better populating the AGN mass range of $M_{\text{BH}} \sim 10^6 - 10^8 M_{\odot}$.

4 DISCUSSION

To test the usefulness of the $M_{\text{BH}} - \tau_{\text{DRW}}$ relation, we obtained host galaxy stellar masses M_* for objects in our final sample when available from Reines & Volonteri (2015). These stellar masses were estimated from Zibetti et al. (2009) mass-to-light ratios as a function of their $g - i$ colors after subtracting the contribution from AGN emission using mock AGN spectra (Reines & Volonteri 2015). We then compared the predicted BH masses from the $M_{\text{BH}} - \tau_{\text{DRW}}$ relation of Burke et al. (2021), $M_{\text{BH},\tau_{\text{DRW}}}$, to the expectation from the $M_{\text{BH}} - M_*$ relation. The results are shown in Figure 6.

We find that the BH masses predicted from $M_{\text{BH}} - \tau_{\text{DRW}}$ relation are less precise (intrinsic scatter of $0.46^{+0.09}_{-0.10}$ dex in predicted BH mass but total rms scatter of $0.77^{+0.02}_{-0.01}$ dex) than the $M_{\text{BH}} - M_*$ relation (intrinsic scatter of $0.14^{+0.09}_{-0.06}$ dex with total rms scatter of $0.51^{+0.01}_{-0.01}$ dex). This intrinsic scatter in predicted BH mass from the $M_{\text{BH}} - \tau_{\text{DRW}}$ relation is broadly consistent with the intrinsic scatter of $0.33^{+0.11}_{-0.11}$ dex found by Burke et al. (2021), and similar to

the scatter in single-epoch virial BH masses (Shen 2013). The larger total rms scatter could be due to the larger measurement uncertainties in our ZTF damping timescale measurements from poorer light curve quality. The BH mass prediction is proportional to $\tau_{\text{DRW}}^{2.54}$, hence a 0.2 dex measurement uncertainty in τ_{DRW} translates to ~ 0.5 dex uncertainty in BH mass, leading to the large rms scatter seen in Figure 6. Given such large measurement uncertainties in predicted BH mass, the nominal intrinsic scatter constrained from the regression fit in this work is more difficult to constrain. Therefore, with higher quality light curves of dwarf AGNs, we expect the predicted BH masses to improve. Alternatively, the large scatter could be due to larger variations of other parameters in dwarf AGNs which were unaccounted for, such as black hole spin and accretion rate. Notably, the Greene & Ho (2007) sample, which may have systematically longer damping timescales in Figure 6, have relatively high Eddington ratios of $\log(L_{\text{bol}}/L_{\text{Edd}}) \sim -0.5$ (Greene & Ho 2007). Future studies with a sample spanning a large range of Eddington luminosity ratios could help inform this work.

We caution that the single-epoch virial BH masses in this work have a typical systematic uncertainty of ~ 0.4 dex (Shen 2013). For a dwarf AGN, the uncertainty may be even larger, because of enhanced complications from outflows or stellar continuum absorption features to measure the weak broad-line emission from the AGN. In addition, the ZTF data release light curves are generally noisier than composite Stripe 82 light curves adopted in Burke et al. (2021) or light curves from dedicated AGN monitoring programs despite the quality constraints we applied. These sources of systematic uncertainty will contribute to the intrinsic scatter in our relations.

5 CONCLUSION

We have analyzed the characteristic ‘‘damping’’ timescale of a final sample of 79 low-mass (dwarf and Seyfert) AGNs with virial BH mass estimates of $M_{\text{BH}} \sim 10^6 - 10^8 M_{\odot}$ at a redshift range of $z \sim 0 - 0.3$ using ZTF data release 13 with ~ 4 year long light curves with sufficient quality to enable reliable DRW model fitting. Our best-fit linear model is consistent with the Burke et al. (2021) results within 1σ where the IMBH range is better populated by the new ZTF sample. This work demonstrates consistency of dwarf AGN variability with the $M_{\text{BH}} - \tau_{\text{DRW}}$ relation, which indicates their single-epoch virial masses are reasonable on average. Given their short damping timescales, we conclude that the dwarf AGN candidates in our sample may indeed be dwarf AGNs, rather than long-lived transients (Burke et al. 2020) or more massive AGNs. This provides a useful and independent line of evidence for the AGN nature of these sources, even for those with narrow emission line ratios consistent with star formation.

High-quality, long-duration light curves will improve the uncertainties on individual τ_{DRW} measurements and improve the robustness of the $M_{\text{BH}} - \tau_{\text{DRW}}$ relation, particularly at the high-mass end ($M_{\text{BH}} \gtrsim 10^9 M_{\odot}$) where exclusion of AGNs with τ_{DRW} values greater than several hundred days with insufficient light curve baselines may result in a slope slightly shallower than the predicted slope of 0.5 from the standard model of accretion disks (Burke et al. 2021).

High-cadence monitoring of the lowest-mass dwarf AGNs ($M_{\text{BH}} \lesssim 10^5 M_{\odot}$) can be used to estimate the BH mass without the need for spectroscopy. The $M_{\text{BH}} - \tau_{\text{DRW}}$ of Burke et al. (2021) relation predicts a damping timescale of about 13 hours (3 days) for a $10^2 M_{\odot}$ ($10^4 M_{\odot}$) IMBH. In this case, the $M_{\text{BH}} - \tau_{\text{DRW}}$ relation can serve as a discovery machine for IMBHs which fail to produce a broad line region (Chakravorty et al. 2014) or where the broad

Table 1. Final sample parameters and variability timing results. We list the J2000 right ascension (RA), declination (DEC), spectroscopic SDSS redshift (z), black hole mass, fitted damping timescale and amplitude, and light curve baseline, Ljung–Box test significance (σ_{LB}), and signal to noise ratio (SNR) as defined in §2.4 in the text. σ_{LB} values of “inf” indicates a high significance beyond the numerical precision limits of our code. The reference refers to the source of the broad-line BH mass estimate we adopted. Logarithms are 10 based.

Used Name	RA (deg)	DEC (deg)	z	$\log(M_{BH}/M_{\odot})$ (dex)	$\log(\tau_{DRW}/\text{days})$ (dex)	$\log(\sigma_{DRW}/\text{mag})$ (dex)	baseline (days)	σ_{LB}	SNR	reference
Liu+18 5	122.29468	11.10531	0.0526	5.95 ± 0.3	1.2 ± 0.1	-1.5 ± 0.4	1505	17.0	1.4	Liu et al. (2018)
Liu+18 33	143.53584	17.94556	0.0271	5.69 ± 0.3	1.6 ± 0.2	-1.4 ± 0.4	1512	26.3	1.5	Liu et al. (2018)
Liu+18 34	143.77839	14.97909	0.0831	6.04 ± 0.3	1.9 ± 0.3	-1.6 ± 0.5	1512	20.1	1.4	Liu et al. (2018)
Liu+18 100	188.65214	16.53123	0.0736	6.14 ± 0.3	1.8 ± 0.2	-1.2 ± 0.4	1553	inf	2.9	Liu et al. (2018)
Liu+18 116	196.20814	20.64553	0.0644	6.17 ± 0.3	1.8 ± 0.3	-1.5 ± 0.5	1561	33.6	1.6	Liu et al. (2018)
Liu+18 117	196.23734	39.92492	0.0274	5.90 ± 0.3	1.3 ± 0.1	-1.7 ± 0.4	1563	inf	1.1	Liu et al. (2018)
Liu+18 125	200.32909	30.07328	0.0916	6.28 ± 0.3	1.8 ± 0.2	-1.4 ± 0.4	1564	inf	1.5	Liu et al. (2018)
Liu+18 126	201.16139	29.17003	0.0727	6.27 ± 0.3	1.7 ± 0.2	-1.4 ± 0.5	1563	inf	1.6	Liu et al. (2018)
Liu+18 157	218.54809	16.84901	0.0936	6.20 ± 0.3	1.8 ± 0.3	-1.5 ± 0.5	1564	inf	1.3	Liu et al. (2018)
Liu+18 173	226.26005	13.03378	0.2045	6.19 ± 0.3	2.1 ± 0.4	-1.7 ± 0.5	1562	31.5	1.1	Liu et al. (2018)
Liu+18 186	238.10368	4.29062	0.0459	6.27 ± 0.3	2.0 ± 0.3	-1.5 ± 0.5	1563	31.8	1.2	Liu et al. (2018)
Liu+18 199	248.75609	30.90337	0.0543	6.27 ± 0.3	1.7 ± 0.2	-1.5 ± 0.4	1562	inf	2.5	Liu et al. (2018)
GH07 60	132.96933	52.47582	0.0644	6.20 ± 0.3	1.6 ± 0.2	-1.8 ± 0.4	1515	inf	1.1	Greene & Ho (2007)
GH07 63	135.83736	4.96059	0.0567	6.10 ± 0.3	1.7 ± 0.2	-1.4 ± 0.5	1512	19.5	1.9	Greene & Ho (2007)
GH07 105	165.74471	46.63652	0.1490	6.10 ± 0.3	1.9 ± 0.2	-1.7 ± 0.5	1538	37.7	1.3	Greene & Ho (2007)
GH07 124	174.15992	42.76473	0.0710	6.00 ± 0.3	1.2 ± 0.1	-1.7 ± 0.4	1540	inf	1.1	Greene & Ho (2007)
GH07 160	199.86049	10.93638	0.0644	5.90 ± 0.3	1.8 ± 0.2	-1.6 ± 0.5	1563	29.3	1.4	Greene & Ho (2007)
GH07 171	209.35217	65.41832	0.1060	6.20 ± 0.3	1.8 ± 0.2	-1.4 ± 0.5	1563	inf	2.2	Greene & Ho (2007)
GH07 177	215.32969	63.21673	0.1340	6.20 ± 0.3	1.7 ± 0.2	-1.6 ± 0.5	1563	inf	1.5	Greene & Ho (2007)
GH07 203	239.79010	35.02988	0.0310	6.20 ± 0.3	1.6 ± 0.1	-1.1 ± 0.4	1564	inf	3.2	Greene & Ho (2007)
GH07 204	240.18746	50.87044	0.1000	6.10 ± 0.3	1.6 ± 0.1	-1.8 ± 0.4	1562	inf	1.1	Greene & Ho (2007)
GH07 215	254.15411	37.24434	0.0626	6.30 ± 0.3	1.1 ± 0.1	-1.6 ± 0.4	1562	inf	2.3	Greene & Ho (2007)
GH07 219	314.59226	-6.83455	0.0737	6.20 ± 0.3	2.1 ± 0.6	-1.4 ± 0.5	1506	23.8	1.3	Greene & Ho (2007)
RV15 4	32.54789	-9.05987	0.0419	8.11 ± 0.5	1.8 ± 0.3	-1.9 ± 0.5	1303	22.8	1.1	Reines & Volonteri (2015)
RV15 6	46.07405	0.47423	0.0447	6.50 ± 0.5	1.8 ± 0.3	-1.4 ± 0.5	1315	inf	1.4	Reines & Volonteri (2015)
RV15 7	50.02634	40.36628	0.0479	6.72 ± 0.5	1.4 ± 0.1	-1.7 ± 0.4	1553	34.8	1.1	Reines & Volonteri (2015)
RV15 12	118.85534	39.18606	0.0333	6.74 ± 0.5	0.9 ± 0.1	-1.3 ± 0.4	1508	inf	2.4	Reines & Volonteri (2015)
RV15 14	119.70951	9.58909	0.0455	7.25 ± 0.5	1.7 ± 0.2	-1.4 ± 0.5	1505	inf	1.3	Reines & Volonteri (2015)
RV15 17	120.68084	31.06759	0.0410	7.80 ± 0.5	2.1 ± 0.3	-1.1 ± 0.5	1506	inf	1.9	Reines & Volonteri (2015)
RV15 21	122.00730	38.32648	0.0413	6.46 ± 0.5	1.1 ± 0.1	-1.8 ± 0.4	1508	31.2	1.0	Reines & Volonteri (2015)
RV15 23	123.33051	46.14712	0.0539	7.08 ± 0.5	1.7 ± 0.2	-1.2 ± 0.4	1496	inf	3.6	Reines & Volonteri (2015)
RV15 26	124.36005	10.20281	0.0455	7.40 ± 0.5	2.2 ± 0.4	-0.9 ± 0.5	1505	inf	1.4	Reines & Volonteri (2015)
RV15 37	131.72539	25.37009	0.0506	7.73 ± 0.5	1.7 ± 0.2	-1.0 ± 0.5	1507	30.5	1.8	Reines & Volonteri (2015)
RV15 45	139.14301	17.91898	0.0268	7.40 ± 0.5	1.2 ± 0.1	-1.7 ± 0.4	1512	21.6	1.8	Reines & Volonteri (2015)
RV15 47	140.31484	10.29473	0.0390	7.36 ± 0.5	1.7 ± 0.3	-1.6 ± 0.5	1512	4.9	2.8	Reines & Volonteri (2015)
RV15 56	145.51997	23.68526	0.0211	7.10 ± 0.5	2.1 ± 0.4	-1.3 ± 0.5	1512	inf	1.5	Reines & Volonteri (2015)
RV15 58	146.37234	9.60290	0.0137	6.35 ± 0.5	1.3 ± 0.2	-1.6 ± 0.4	1512	22.5	2.3	Reines & Volonteri (2015)
RV15 68	150.52930	3.05767	0.0228	7.22 ± 0.5	1.6 ± 0.2	-1.4 ± 0.4	1513	31.3	4.5	Reines & Volonteri (2015)
RV15 69	150.57826	26.80159	0.0518	7.52 ± 0.5	1.4 ± 0.2	-1.6 ± 0.4	1515	inf	2.1	Reines & Volonteri (2015)
RV15 73	153.01080	30.21751	0.0497	7.29 ± 0.5	1.8 ± 0.2	-1.3 ± 0.5	1523	inf	1.3	Reines & Volonteri (2015)
RV15 83	159.46589	33.81392	0.0510	6.43 ± 0.5	1.5 ± 0.2	-1.7 ± 0.4	1523	28.0	1.1	Reines & Volonteri (2015)
RV15 85	160.72055	4.24476	0.0519	7.29 ± 0.5	1.8 ± 0.3	-1.4 ± 0.5	1529	26.9	1.8	Reines & Volonteri (2015)
RV15 92	165.06680	46.27092	0.0315	6.44 ± 0.5	1.5 ± 0.1	-1.5 ± 0.4	1538	inf	2.4	Reines & Volonteri (2015)
RV15 98	167.69151	11.61153	0.0417	7.18 ± 0.5	1.4 ± 0.2	-1.5 ± 0.4	1527	15.7	1.1	Reines & Volonteri (2015)
RV15 102	169.74039	58.05665	0.0282	7.10 ± 0.5	1.4 ± 0.2	-1.5 ± 0.4	1540	inf	1.8	Reines & Volonteri (2015)
RV15 106	171.61964	47.41495	0.0331	6.35 ± 0.5	2.1 ± 0.3	-1.6 ± 0.5	1540	inf	1.3	Reines & Volonteri (2015)
RV15 113	175.05809	24.69706	0.0127	7.00 ± 0.5	2.1 ± 0.5	-1.9 ± 0.5	1538	33.1	1.6	Reines & Volonteri (2015)
RV15 119	176.43826	55.79998	0.0540	7.16 ± 0.5	1.2 ± 0.1	-2.0 ± 0.4	1547	inf	1.3	Reines & Volonteri (2015)
RV15 122	179.29451	22.29617	0.0520	7.30 ± 0.5	1.9 ± 0.3	-1.5 ± 0.5	1547	27.4	2.3	Reines & Volonteri (2015)
RV15 123	180.30980	-3.67809	0.0193	6.96 ± 0.5	1.7 ± 0.3	-1.4 ± 0.5	1536	10.8	1.8	Reines & Volonteri (2015)
RV15 129	181.60947	42.74056	0.0522	7.33 ± 0.5	1.8 ± 0.2	-1.1 ± 0.5	1549	inf	3.7	Reines & Volonteri (2015)
RV15 130	181.86655	25.60303	0.0481	6.64 ± 0.5	1.5 ± 0.1	-1.6 ± 0.4	1545	inf	1.5	Reines & Volonteri (2015)
RV15 133	184.02951	50.82512	0.0313	8.06 ± 0.5	2.0 ± 0.3	-0.9 ± 0.5	1553	inf	2.5	Reines & Volonteri (2015)
RV15 134	184.61134	-0.13059	0.0499	6.56 ± 0.5	1.5 ± 0.2	-1.7 ± 0.4	1545	12.9	1.7	Reines & Volonteri (2015)
RV15 137	185.56405	28.35659	0.0277	6.84 ± 0.5	1.4 ± 0.1	-1.4 ± 0.4	1551	inf	1.6	Reines & Volonteri (2015)
RV15 140	188.15618	66.41459	0.0473	7.40 ± 0.5	1.3 ± 0.1	-1.1 ± 0.4	1563	inf	2.8	Reines & Volonteri (2015)
RV15 152	195.08309	61.65512	0.0526	7.60 ± 0.5	1.3 ± 0.1	-1.2 ± 0.4	1561	inf	3.3	Reines & Volonteri (2015)
RV15 157	198.27422	1.46553	0.0288	6.44 ± 0.5	2.0 ± 0.3	-1.5 ± 0.5	1563	25.0	2.1	Reines & Volonteri (2015)
RV15 164	204.41614	39.15456	0.0202	6.70 ± 0.5	1.6 ± 0.2	-1.8 ± 0.4	1563	inf	1.4	Reines & Volonteri (2015)
RV15 167	206.11005	44.27223	0.0546	6.82 ± 0.5	1.5 ± 0.1	-1.1 ± 0.4	1564	inf	2.0	Reines & Volonteri (2015)
RV15 174	211.31193	-2.98367	0.0535	7.21 ± 0.5	1.5 ± 0.2	-1.6 ± 0.4	1559	16.8	1.4	Reines & Volonteri (2015)
RV15 176	214.12843	1.61890	0.0536	7.22 ± 0.5	1.6 ± 0.2	-1.4 ± 0.4	1564	32.9	2.7	Reines & Volonteri (2015)
RV15 177	214.49809	25.13687	0.0167	7.94 ± 0.5	2.1 ± 0.3	-0.3 ± 0.5	1564	inf	1.1	Reines & Volonteri (2015)
RV15 180	216.03493	21.08848	0.0471	7.03 ± 0.5	1.7 ± 0.2	-1.4 ± 0.5	1564	inf	1.9	Reines & Volonteri (2015)
RV15 186	222.73097	27.57853	0.0303	6.79 ± 0.5	1.6 ± 0.2	-1.5 ± 0.4	1563	30.2	1.7	Reines & Volonteri (2015)
RV15 191	225.41164	10.42040	0.0302	7.07 ± 0.5	1.7 ± 0.2	-1.2 ± 0.4	1564	inf	1.5	Reines & Volonteri (2015)
RV15 200	230.85180	55.31542	0.0394	6.72 ± 0.5	1.9 ± 0.2	-1.9 ± 0.5	1564	inf	1.0	Reines & Volonteri (2015)
RV15 202	232.41909	30.48592	0.0359	6.97 ± 0.5	1.8 ± 0.2	-1.5 ± 0.5	1564	inf	1.2	Reines & Volonteri (2015)
RV15 211	238.57264	32.64387	0.0486	7.73 ± 0.5	1.5 ± 0.1	-1.3 ± 0.4	1564	inf	2.4	Reines & Volonteri (2015)
RV15 212	239.17043	12.28831	0.0355	6.66 ± 0.5	1.5 ± 0.2	-1.6 ± 0.4	1562	31.9	1.6	Reines & Volonteri (2015)
RV15 215	241.26026	33.09584	0.0532	7.80 ± 0.5	1.6 ± 0.1	-1.3 ± 0.4	1563	inf	3.9	Reines & Volonteri (2015)
RV15 220	242.98464	52.18809	0.0416	7.26 ± 0.5	1.5 ± 0.1	-1.4 ± 0.4	1562	inf	2.1	Reines & Volonteri (2015)
RV15 223	244.68689	25.65212	0.0483	7.20 ± 0.5	1.5 ± 0.1	-1.3 ± 0.4	1563	inf	2.0	Reines & Volonteri (2015)
RV15 224	244.96380	40.97981	0.0383	6.78 ± 0.5	1.8 ± 0.2	-1.0 ± 0.5	1563	inf	4.2	Reines & Volonteri (2015)
RV15 228	247.53080	-0.19345	0.0467	7.14 ± 0.5	1.3 ± 0.1	-1.7 ± 0.4	1555	8.3	1.3	Reines & Volonteri (2015)
RV15 233	258.11851	35.88406	0.0269	6.97 ± 0.5	2.0 ± 0.3	-1.5 ± 0.5	1562	inf	2.2	Reines & Volonteri (2015)
RV15 236	316.38934	0.47478	0.0549	6.49 ± 0.5	1.6 ± 0.2	-1.6 ± 0.4	1532	25.2	1.4	Reines & Volonteri (2015)
RV15 238	323.43439	-8.27101	0.0533	7.57 ± 0.5	1.5 ± 0.2	-1.8 ± 0.4	1503	7.9	1.1	Reines & Volonteri (2015)
RV15 242	342.10264	0.15573	0.0544	6.62 ± 0.5	1.3 ± 0.1	-1.6 ± 0.4	1496	20.8	1.2	Reines & Volonteri (2015)

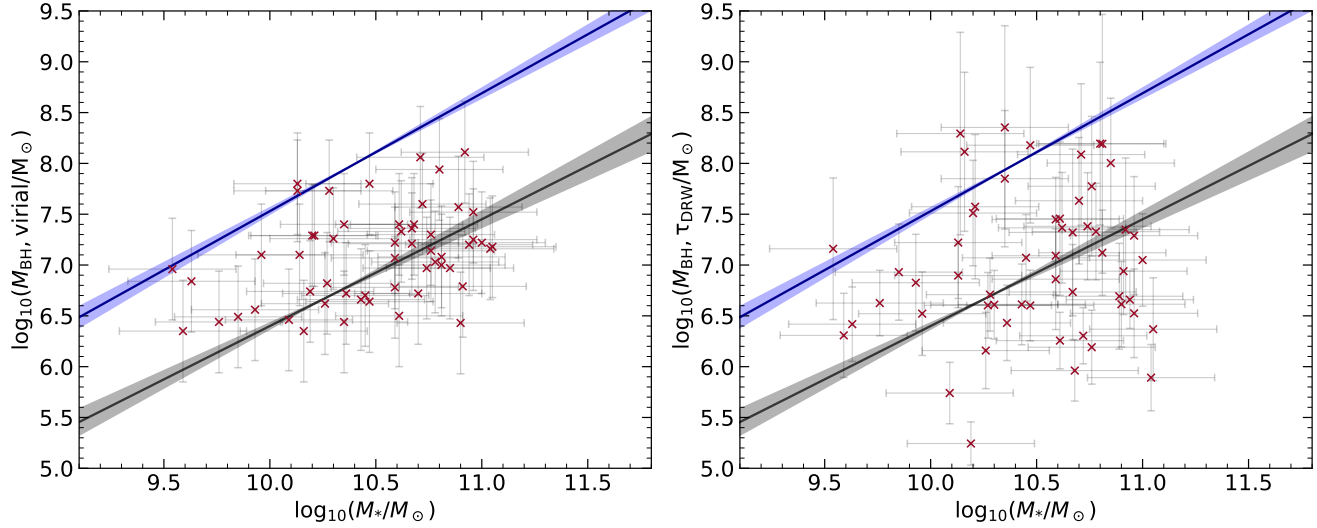


Figure 6. Comparison between $M_{\text{BH}} - M_*$ and $M_{\text{BH}} - \tau_{\text{DRW}}$ relations. We plot the virial BH mass $M_{\text{BH,virial}}$ versus M_* against the relations of Reines & Volonteri (2015) and Kormendy & Ho (2013) (left). We also plot the BH mass predicted from the $M_{\text{BH}} - \tau_{\text{DRW}}$ relation of Burke et al. (2021) using our ZTF light curves versus the stellar masses from Reines & Volonteri (2015) in the g band (right). The gray (blue) line and shaded band is the best-fit local AGN scaling relation and 1σ uncertainty from Reines & Volonteri (2015) (Kormendy & Ho (2013)) relations. The fitted intrinsic scatter of our data in each panel is, from left to right: $0.14^{+0.09}_{-0.06}$ and $0.46^{+0.09}_{-0.10}$ dex.

emission line is too weak to detect, as long as the optical variability is dominated by the accretion disk emission rather than from a companion star or reprocessed light from X-rays. This motivates optical surveys with intra-day cadence to enable discovery and mass estimation of IMBHs using variability (Bellm et al. 2022). The variable sky at these timescales is still relatively unexplored at sufficient volumes and depths to enable a systematic search for rapidly-accreting IMBHs.

ACKNOWLEDGEMENTS

We thank Gautham Narayan for useful discussions. C.J.B. acknowledges the Illinois Graduate Survey Science Fellowship for partial support. Z.F.W. and X.L. acknowledge support from the University of Illinois Campus Research Board and NSF grant AST-2206499. Y.S. acknowledges support from NSF grant AST-2009947. This research was supported in part by the National Science Foundation under PHY-1748958. This research made use of Photutils, an Astropy package for detection and photometry of astronomical sources (Bradley et al. 2022).

Based on observations obtained with the Samuel Oschin Telescope 48-inch and the 60-inch Telescope at the Palomar Observatory as part of the Zwicky Transient Facility project. ZTF is supported by the National Science Foundation under Grant No. AST-2034437 and a collaboration including Caltech, IPAC, the Weizmann Institute for Science, the Oskar Klein Center at Stockholm University, the University of Maryland, Deutsches Elektronen-Synchrotron and Humboldt University, the TANGO Consortium of Taiwan, the University of Wisconsin at Milwaukee, Trinity College Dublin, Lawrence Livermore National Laboratories, and IN2P3, France. Operations are conducted by COO, IPAC, and UW.

This work makes use of SDSS-I/II and SDSS-III/IV data (<http://www.sdss.org/> and <http://www.sdss3.org/>).

Facilities: ZTF, Sloan

DATA AVAILABILITY

All ZTF light curves can be downloaded at <https://irsa.ipac.caltech.edu/Missions/ztf.html>. Our timing analysis code is available at <https://github.com/burke86/taufit>.

REFERENCES

- Abazajian K. N., et al., 2009, *ApJS*, **182**, 543
- Aigrain S., Foreman-Mackey D., 2022, arXiv e-prints, p. [arXiv:2209.08940](https://arxiv.org/abs/2209.08940)
- Baldassare V. F., Reines A. E., Gallo E., Greene J. E., 2015, *ApJ*, **809**, L14
- Baldassare V. F., et al., 2016, *ApJ*, **829**, 57
- Baldassare V. F., Geha M., Greene J., 2018, *ApJ*, **868**, 152
- Baldassare V. F., Geha M., Greene J., 2020, *ApJ*, **896**, 10
- Baldwin J. A., Phillips M. M., Terlevich R., 1981, *PASP*, **93**, 5
- Bellm E. C., et al., 2019, *PASP*, **131**, 018002
- Bellm E. C., Burke C. J., Coughlin M. W., Andreoni I., Raiteri C. M., Bonito R., 2022, *ApJS*, **258**, 13
- Bradley L., et al., 2022, astropy/photutils: 1.5.0, doi:10.5281/zenodo.6825092, <https://doi.org/10.5281/zenodo.6825092>
- Burke C. J., et al., 2020, *ApJ*, **894**, L5
- Burke C. J., et al., 2021, *Science*, **373**, 789
- Burke C. J., et al., 2022, *MNRAS*, **516**, 2736
- Cann J. M., Satyapal S., Abel N. P., Ricci C., Secret N. J., Blecha L., Gliozzi M., 2018, *ApJ*, **861**, 142
- Cann J. M., et al., 2020, *ApJ*, **895**, 147
- Chakravorty S., Elvis M., Ferland G., 2014, *MNRAS*, **437**, 740
- Chilingarian I. V., Katkov I. Y., Zolotukhin I. Y., Grishin K. A., Beletsky Y., Boutsia K., Osip D. J., 2018, *ApJ*, **863**, 1
- Farrell S. A., Webb N. A., Barret D., Godet O., Rodrigues J. M., 2009, *Nature*, **460**, 73
- Foreman-Mackey D., Hogg D. W., Lang D., Goodman J., 2013, *PASP*, **125**, 306
- Foreman-Mackey D., Agol E., Ambikasaran S., Angus R., 2017, *AJ*, **154**, 220
- Graham A. W., Driver S. P., Petrosian V., Conselice C. J., Bershadsky M. A., Crawford S. M., Goto T., 2005, *AJ*, **130**, 1535
- Greene J. E., Ho L. C., 2005, *ApJ*, **630**, 122

- Greene J. E., Ho L. C., 2007, [ApJ](#), **670**, 92
 Greene J. E., Strader J., Ho L. C., 2020, [ARA&A](#), **58**, 257
 Guo H., et al., 2020, [MNRAS](#), **496**, 3636
 Inayoshi K., Visbal E., Haiman Z., 2020, [ARA&A](#), **58**, 27
 Kasliwal V. P., Vogeley M. S., Richards G. T., 2015, [MNRAS](#), **451**, 4328
 Kelly B. C., 2007, [ApJ](#), **665**, 1489
 Kelly B. C., Bechtold J., Siemiginowska A., 2009, [ApJ](#), **698**, 895
 Kelly B. C., Becker A. C., Sobolewska M., Siemiginowska A., Uttley P., 2014, [ApJ](#), **788**, 33
 Kewley L. J., Groves B., Kauffmann G., Heckman T., 2006, [MNRAS](#), **372**, 961
 Kormendy J., Ho L. C., 2013, [ARA&A](#), **51**, 511
 Kozłowski S., 2017, [A&A](#), **597**, A128
 LIGO Scientific Collaboration Virgo Collaboration 2020, [Phys. Rev. Lett.](#), **125**, 101102
 Lin D., et al., 2018, [Nature Astronomy](#), **2**, 656
 Liu H.-Y., Yuan W., Dong X.-B., Zhou H., Liu W.-J., 2018, [ApJS](#), **235**, 40
 Ljung G. M., Box G. E. P., 1978, [Biometrika](#), **65**, 297
 Lomb N. R., 1976, [Ap&SS](#), **39**, 447
 MacLeod C. L., et al., 2010, [ApJ](#), **721**, 1014
 Martínez-Palomera J., Lira P., Bhalla-Ladd I., Förster F., Plotkin R. M., 2020, [ApJ](#), **889**, 113
 Masci F. J., et al., 2019, [PASP](#), **131**, 018003
 Mushotzky R. F., Edelson R., Baumgartner W., Gandhi P., 2011, [ApJ](#), **743**, L12
 Petrosian V., 1976, [ApJ](#), **210**, L53
 Reines A. E., Comastri A., 2016, [Publ. Astron. Soc. Australia](#), **33**, e054
 Reines A. E., Volonteri M., 2015, [ApJ](#), **813**, 82
 Reines A. E., Greene J. E., Geha M., 2013, [ApJ](#), **775**, 116
 Scargle J. D., 1982, [ApJ](#), **263**, 835
 Scaringi S., et al., 2015, [Science Advances](#), **1**, e1500686
 Shen Y., 2013, [Bulletin of the Astronomical Society of India](#), **41**, 61
 Simm T., Salvato M., Saglia R., Ponti G., Lanzuisi G., Trakhtenbrot B., Nandra K., Bender R., 2016, [A&A](#), **585**, A129
 Stone Z., et al., 2022, [MNRAS](#), **514**, 164
 Suberlak K. L., Ivezić Ž., MacLeod C., 2021, [ApJ](#), **907**, 96
 Veilleux S., Osterbrock D. E., 1987, [ApJS](#), **63**, 295
 Volonteri M., 2010, [A&ARv](#), **18**, 279
 Ward C., et al., 2022, [ApJ](#), **936**, 104
 York D. G., et al., 2000, [AJ](#), **120**, 1579
 Zibetti S., Charlot S., Rix H.-W., 2009, [MNRAS](#), **400**, 1181

APPENDIX A: FINAL SAMPLE LIGHT CURVES AND BEST-FIT DRW MODELS

We show the difference imaging light curves and DRW modeling for all sources in our final, high-quality sample in Figure A1.

This paper has been typeset from a $\text{\TeX}/\text{\LaTeX}$ file prepared by the author.

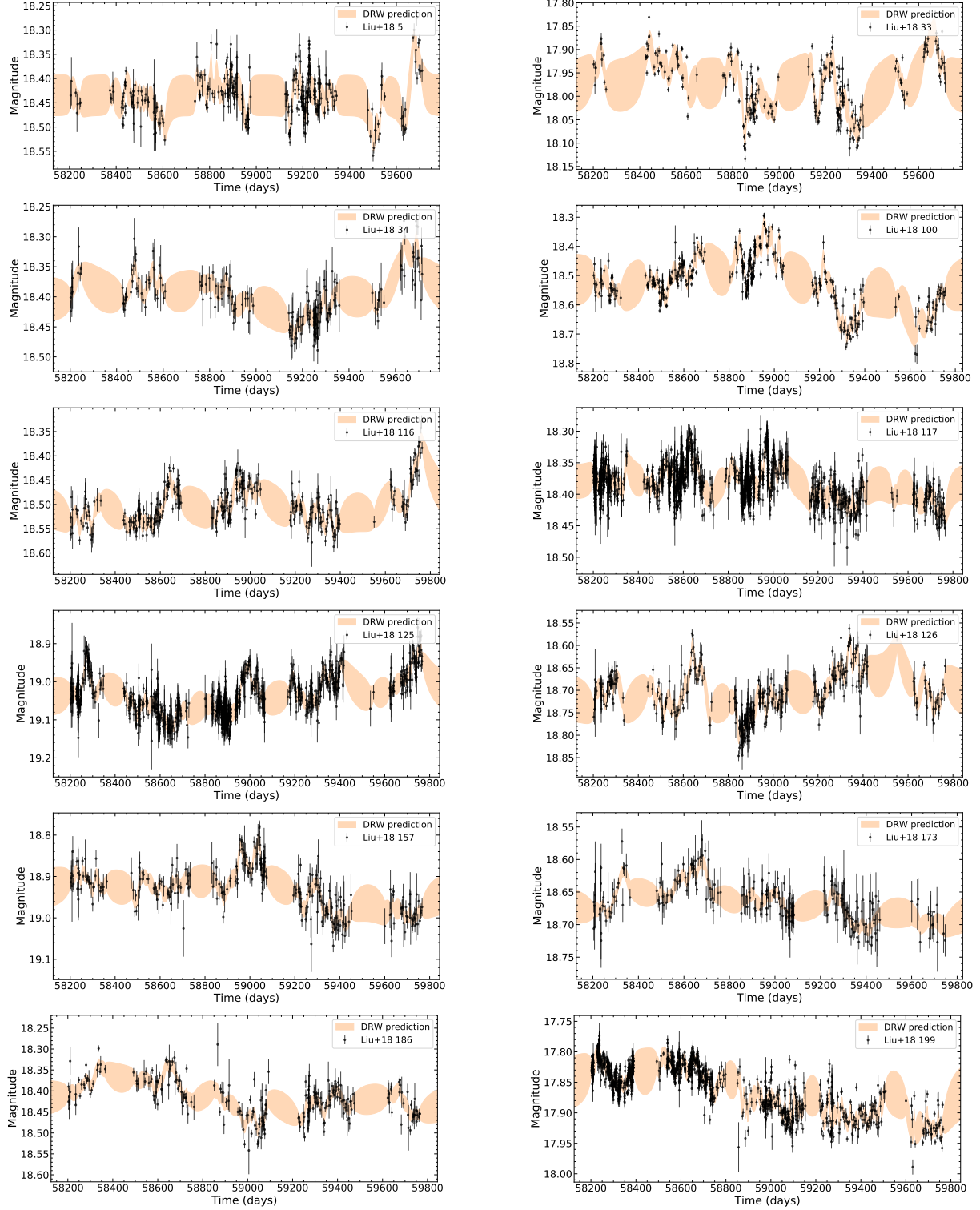
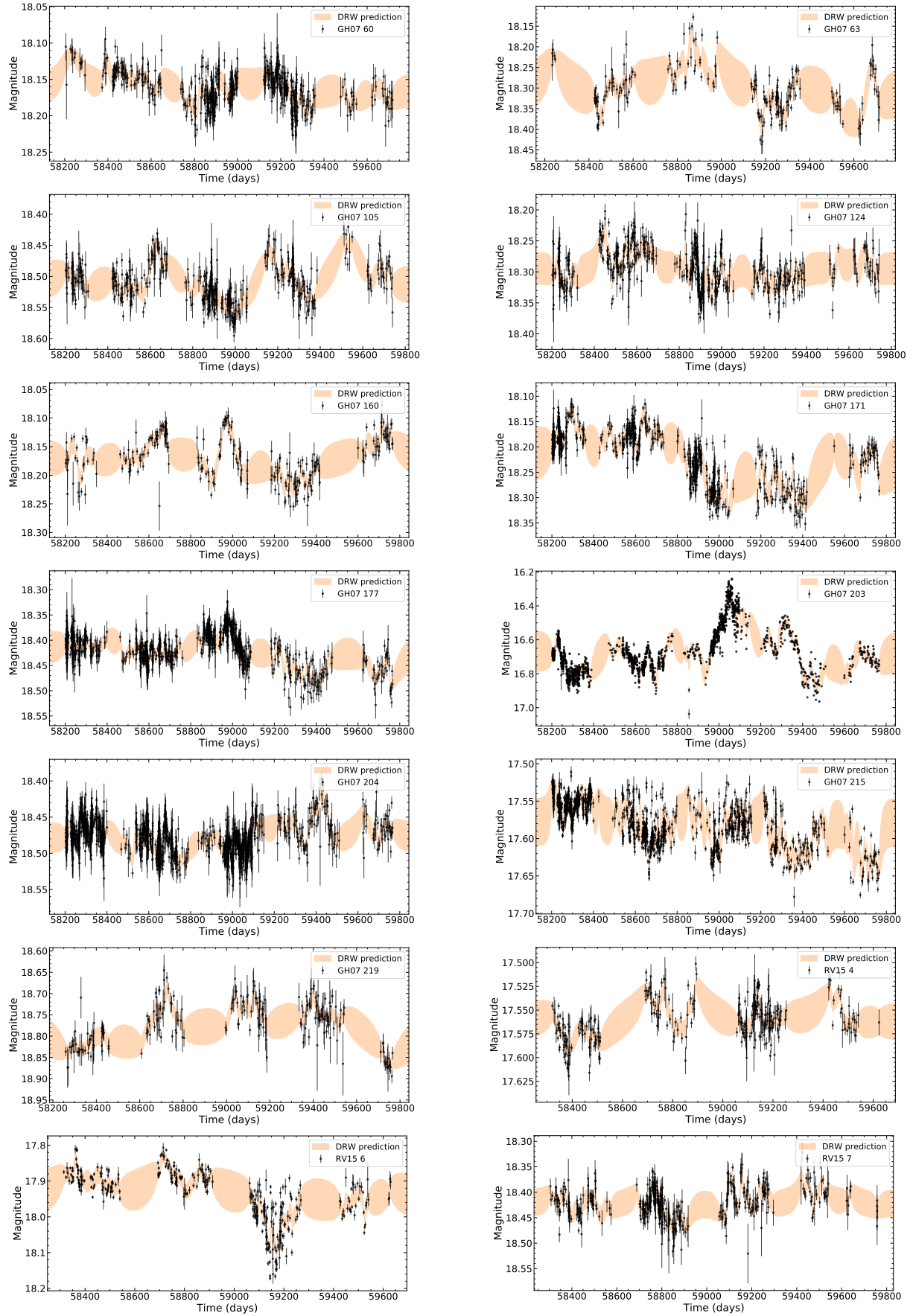
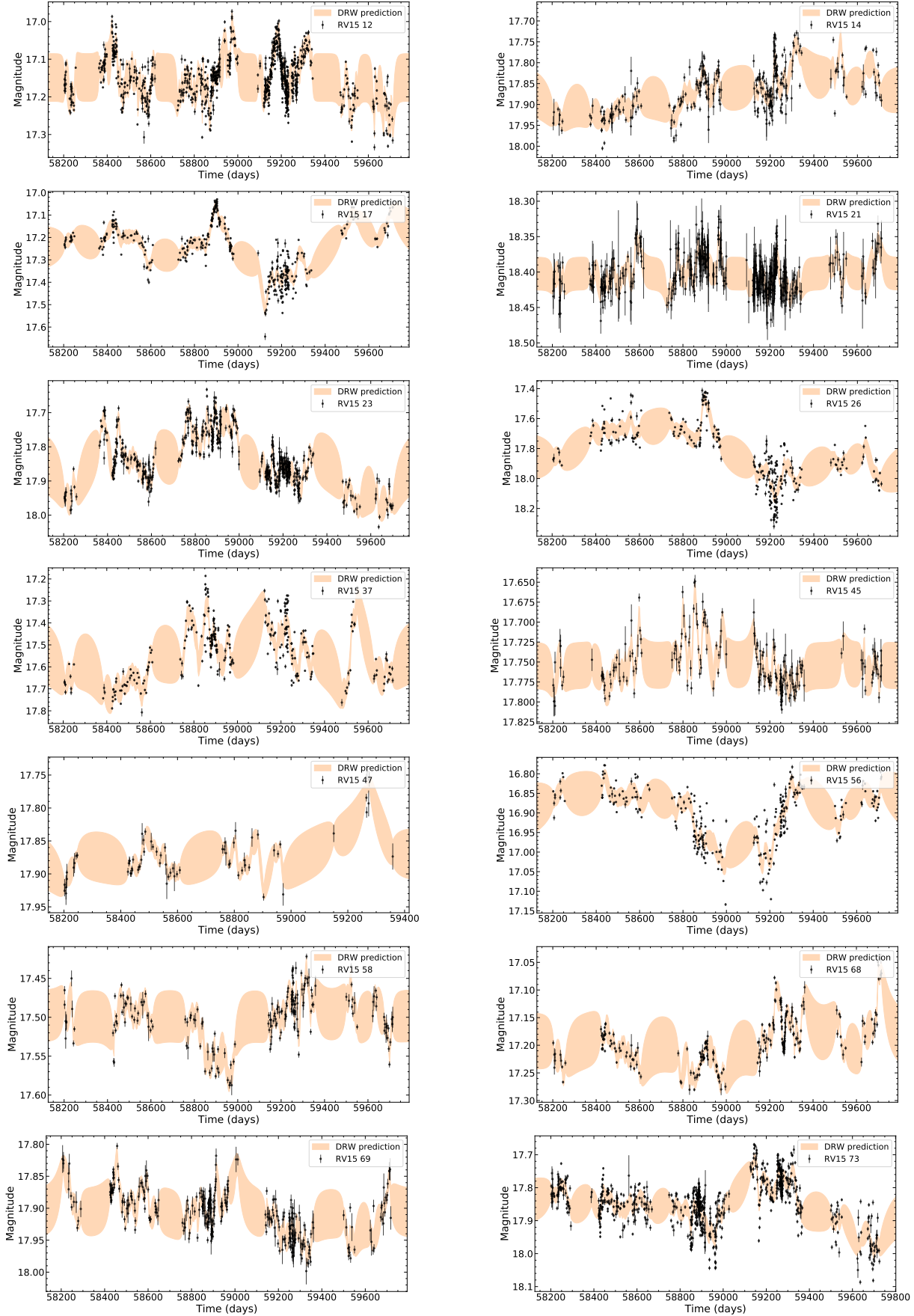


Figure A1. ZTF g -band difference imaging light curves and DRW model predictions for dwarf AGNs in our final sample (continued below).

**Figure A2.** Continuation of Figure A1.

**Figure A3.** Continuation of Figure A1.

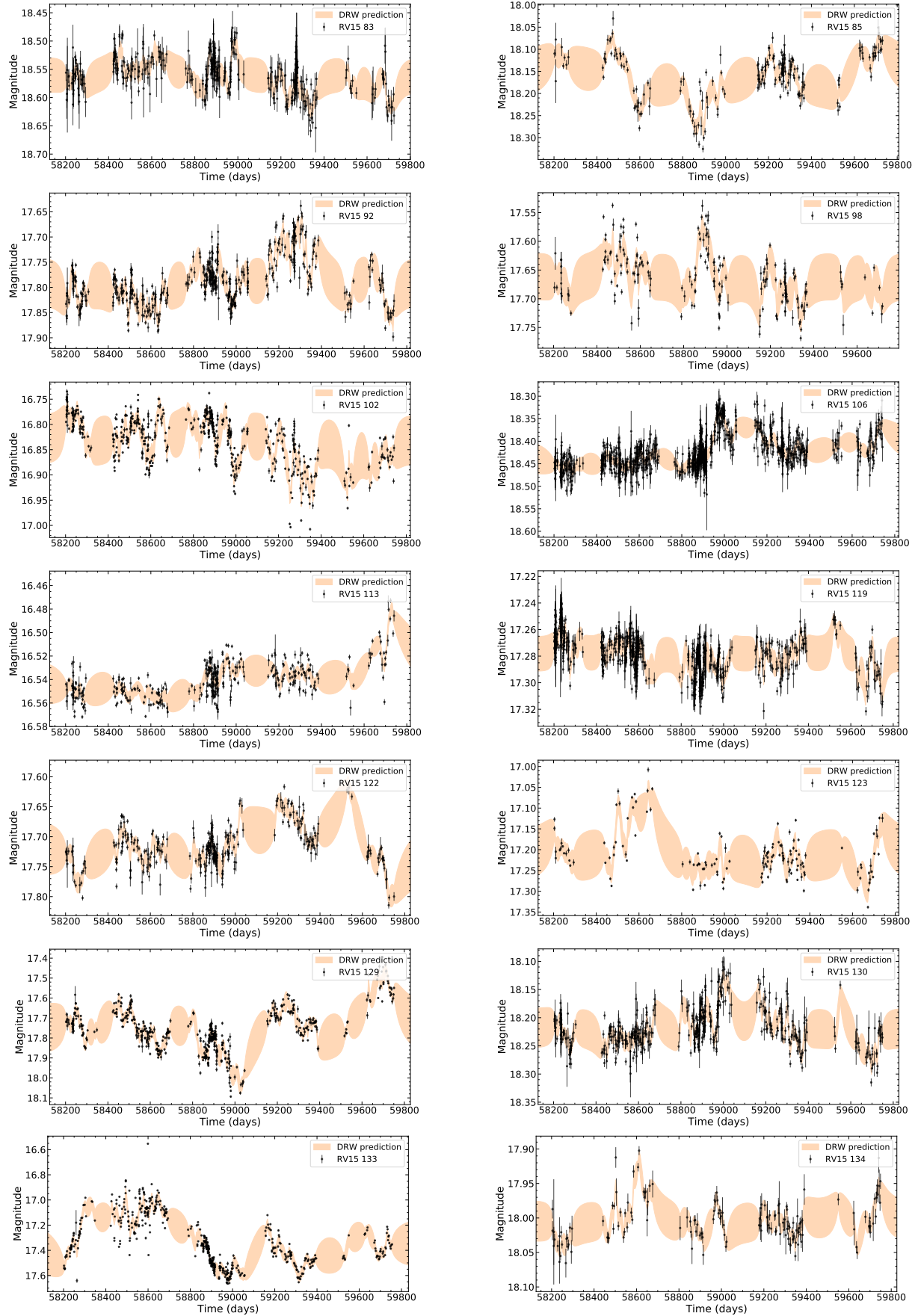
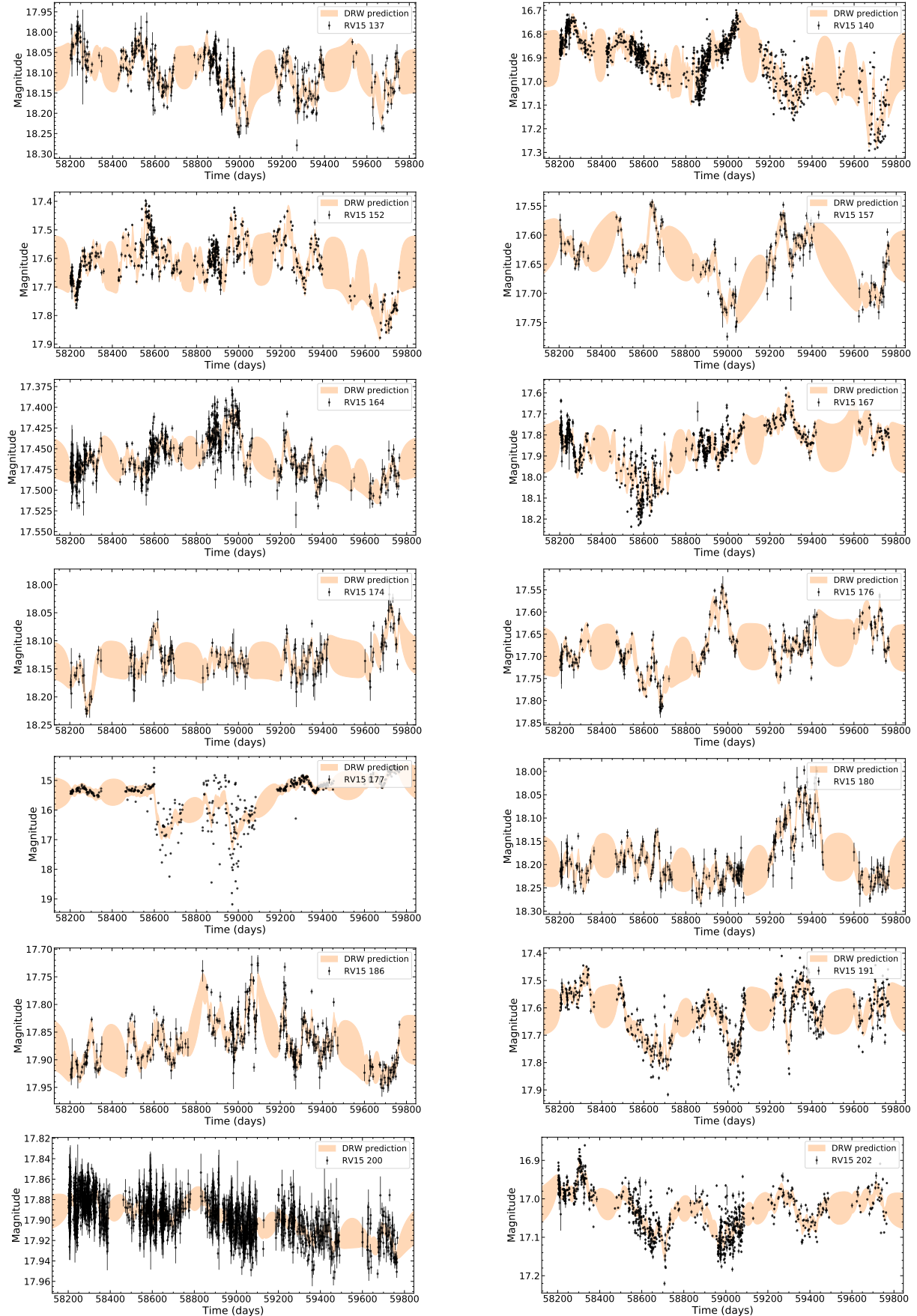
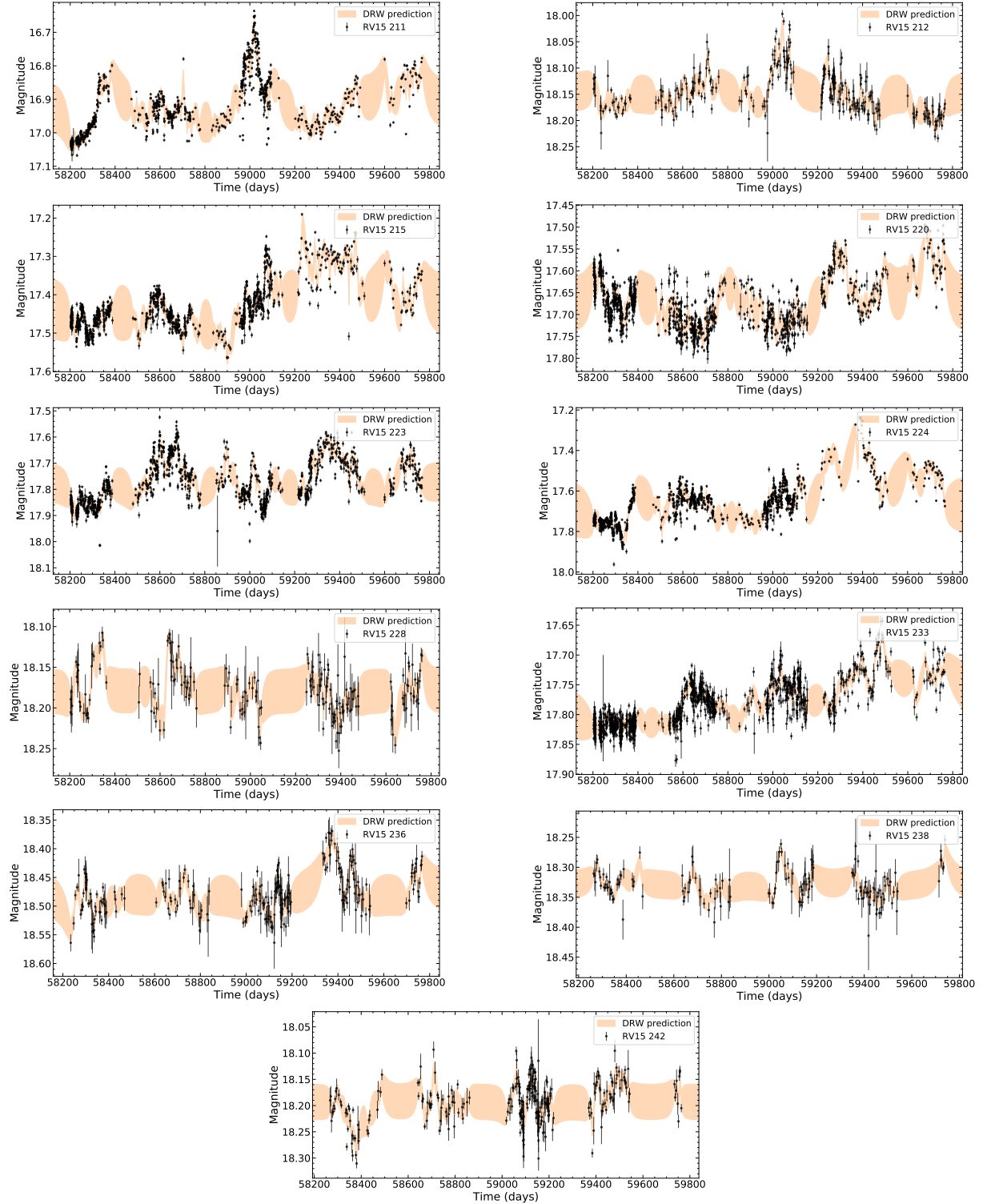


Figure A4. Continuation of Figure A1.

**Figure A5.** Continuation of Figure A1.

**Figure A6.** Continuation of Figure A1.